

GT2011-45116

## SURGE INCEPTION IN A TRANSONIC CENTRIFUGAL COMPRESSOR STAGE

Isabelle Trébinjac\*, Nicolas Bulot\*\*, Xavier Ottavy\*, Nicolas Buffaz\*

\* Laboratoire de Mécanique des Fluides et d'Acoustique, UMR CNRS 5509  
Ecole Centrale de Lyon, UCBLyon I, INSA  
36 av. Guy de Collongue, 69134 Ecully Cedex, France

\*\* TURBOMECA, Groupe SAFRAN  
64511 Bordes, France

### ABSTRACT

Numerical and experimental investigations were conducted in a transonic centrifugal compressor stage composed of a backswept splintered unshrouded impeller and a vaned diffuser. Unsteady 3D simulations were performed with the code *elsA* that solves the turbulent averaged Navier-Stokes equations, at three operating points: choked flow, peak efficiency and near surge. Unsteady pressure measurements up to 150 kHz were carried out in the entry zone of the vaned diffuser (in the vaneless space and in the semi-vaneless space) when the compressor came into surge. These static pressure sensors were mounted on the shroud enwall.

The paper focuses on the vaneless and semi-vaneless space where the surge originates. A detailed analysis of the flow pattern coming from the unsteady computations from choked flow towards surge led to identify the physical mechanisms involved in the surge inception. It is shown that, when approaching surge, the flow is destabilized by a severe modification of the shock system in the vaned diffuser inlet.

The first perturbation is acquired from the transducer located just upstream of the shock foot (i.e. on the vane suction side surface), indicating a movement of the shock towards the vaneless space. This perturbation travels upstream and leads to the strongest short-wavelength perturbation acquired from the transducer located just upstream of the vane leading edge. This strongest short-wavelength perturbation which level may reach almost four times the mean exit pressure value triggers the full scale instability.

### INTRODUCTION

Current engine design tends towards compact, highly efficient and large operability configurations. The operating range of high speed compressors is limited by choking at high mass flow rate and by the onset of instabilities at low mass flow rate. A safety margin, known as the *surge margin*, prevents the compressor from operating close to the stability limit, precisely where the pressure ratio generally reaches its highest level. In order to increase the operating range, there is therefore great interest in precisely predicting the stability limit of the compression system. That requires reaching a comprehensive understanding of the physical phenomena which trigger the instabilities.

Although the instabilities in both axial and centrifugal configurations are similar (rotating stall and surge), centrifugal compressors are characterized by a wider spectrum of unstable behaviour than axial flow compressors. Combined with a complex flow structure that is inherent to centrifugal geometry, it explains why surge inception in centrifugal compressors is less well understood than similar phenomenon in axial compressors.

For a decade, the surge inception in the NASA CC3 high-speed centrifugal compressor has been studied by many research teams. Spakovszky [1, 2] showed that the unsteady blade-row interaction and coupling is driven by the resonant behaviour of the rotor and the stator wave systems. He also stated the existence of backward travelling stall precursors, which was experimentally and numerically confirmed by Wernet et al. [3] and Skoch et al. [4] respectively.

From high frequency pressure measurements, Justen et al. [5] also showed that the diffuser is the component with the

strongest pre-stall activity. Depending on the vaneless space size and the rotation speed, the surge initiates either in the vaneless space or at the diffuser throat. But in both cases, the surge is driven by a local flow structure.

A local flow structure or the growing of pre-stall waves may therefore drive the compression system into surge. That leads the pre-surge behaviour to be dominated either by spikes (short-wavelength disturbance) or by modal waves (long-wavelength perturbation) respectively. In a recent work, Spakovszky and Roduner [6] showed the possibility to switch from one type to the other one in a given compressor by controlling bleed flow at the impeller exit.

In the works which are mentioned above, the diffusers operate with subsonic inlet conditions. Few studies concern supersonic conditions. Let us mention the works of Hayami et al [7, 8] and Bonaiuti et al. [9] in a high-pressure centrifugal compressor (pressure ratio of 7.75:1) for which the surge is triggered by a boundary layer separation in the vane pressure side – hub corner (spike type).

In the present work, on one hand, the diffuser is fully shocked and, on the other hand, the radial gap between the impeller exit and the vaned diffuser inlet is too small to allow a good mixing. Therefore the unsteady processes significantly impact as well the stage performance [10] as the surge inception.

The aim of the present paper is to identify the mechanisms involved in the surge onset focusing on detailed three-dimensional features of the flow in the region of interaction.

In the first part of the paper, the test case is briefly described. Then the experimental and numerical approaches are presented. The three-dimensional flow features in the region of interaction are described. Finally, from the analysis of pressure measurements with high temporal resolution, the path to surge is given.

## NOMENCLATURE

### Latin letters

BLS	Boundary Layer Separation
C	choke
D	diameter
h	section height
$k, l$	kinetic turbulent energy, length scale of turbulence
LDA	Laser Doppler Anemometry
$\dot{m}$	mass flow
M	Mach number
N	number of blades
NS	Near surge
PE	peak efficiency
PS, SS	pressure side, suction side
p	pressure

T	time period, temperature
t	time
$u_\tau^*$	skin friction velocity
U	impeller speed
V	absolute velocity
y	distance from wall
$y^+$	reduced distance from the wall = $\rho y u_\tau^* / \mu$

### Greek letters

$\gamma$	specific heat ratio
$\pi$	pressure ratio
$\rho$	density
$\mu$	molecular dynamic viscosity
$\Omega$	rotation speed

### Superscripts and subscripts

* or red	reduced variable
$\tilde{f}^{RR}$	time-averaged over a rotor revolution value of $f$
t	stagnation value
1	at impeller inlet
2	at impeller exit
3	at diffuser exit
nom	nominal
r	gas constant
R/S	relative to rotor/stator (impeller/diffuser)
t	stagnation value

## TEST CASE

The test case is a centrifugal compressor stage used in a helicopter engine designed and built by Turbomeca. The backswept unshrouded impeller is composed of  $N_R$  main blades and  $N_R$  splitter blades. The vaned diffuser is composed of  $N_S$  vanes. A 3D sketch of the stage is given in Figure 1.

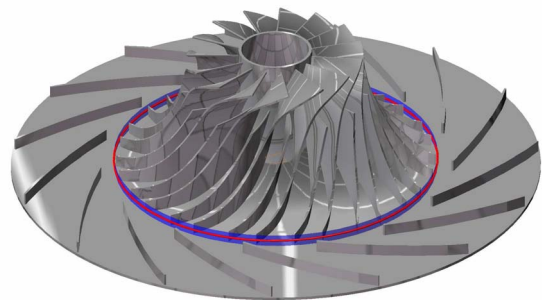


Figure 1. 3D sketch of the centrifugal compressor stage.

The compressor stage is mounted on a 1MW test rig equipped with 67 steady sensors (temperature, pressure, and vibration measurements) dedicated to monitoring and overall performance measuring (Figure 2).

The rotation speed, the flow rate and the measured pressures and temperatures are given at  $\pm 0.1\%$ ,  $\pm 0.5\%$ ,  $\pm 0.05\%$  and  $\pm 1\text{K}$  respectively.



Figure 2. Compressor on the 1MW test rig

The measurements and calculations were performed at a rotation speed  $\Omega_R = 0.927 \cdot \Omega_{nom}$ . At that speed, the rotor runs with subsonic inlet conditions whereas the absolute Mach number at the vaned diffuser inlet is supersonic.

## EXPERIMENTAL PROCEDURE

### Unsteady pressure measurements

Due to the expected time scales within such a high-speed compressor, the acquisition data rate has to be high enough in order to reach a sufficient time resolution of the pressure signal at any given stable operating point, but also high enough in order to record the disturbances which may lead to the onset of instabilities when moving towards surge. Taking this into account, the aim was to measure unsteady pressure with a high level of frequency, typically reaching 150 kHz (i.e. more than fifteen times the main blade passing frequency). A specific unsteady pressure acquisition system has been developed and is presented in Figure 3. This system is split into three parts: the pressure transducer, the signal conditioner - developed in-house - and the digitizing and storing system.

The first part concerns the pressure transducers. Not only the time resolution but also its resistance to high temperature has to be checked. Temperature can be increased by around 350 K in this machine. High frequency response transducers from *Kulite* were chosen, without protective grid. Their natural frequency is around 440 kHz, judging from the results obtained in a shock tube and when mounted in our compressor. This normally permits measurements to be made up to one third of the natural frequency, i.e. in the range [0;145 kHz]. Each Kulite sensor is excited by an accurate DC power supply using batteries and an electronic device developed in-house. The excitation is set to 12 V (instead of the 10 V recommended by the manufacturer) and causes an increase of the sensitivity of 20%, around 35.1 mV/bar for our sensors.

The second part of the unsteady data acquisition system is related to the signal conditioning. Each Kulite pressure transducer is connected with a differential input to a conditioner developed in-house. This conditioner is a precision DC bridge amplifier with a built-in constant excitation voltage/current supply (5V) and a low-pass filter with a cut-off frequency of 250 kHz. Details about this conditioner can be found in the works of Bulot et al. [11].

The third part concerns the digitizing and storing system. The acquisition system was built around the *National Instruments* PXI Modular Instrumentation System. The core of the system is a set of 8 PXI-6123 data acquisition boards with a sampling frequency of 500 kHz. Each board accepts 8 differential analogical inputs, for 8 Kulite connections. The boards have 16-bit resolution and communicate with the data acquisition computer (*Dell T7400*) via 2 communication boards. The files are stored in binary format. Specific software was developed to acquire, store, read and post-treat the data. To perform the voltage/pressure conversion, classical calibrations and zero drift corrections (before and after the tests) were applied.

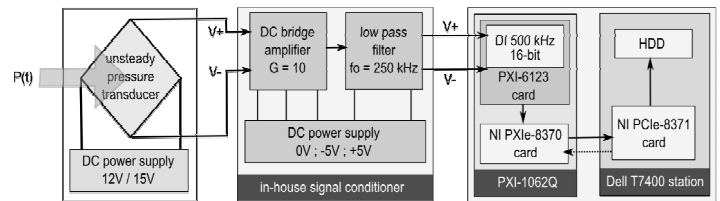


Figure 3. Unsteady data acquisition system.

Figure 4 gives the location of the fifteen pressure sensors at mid inter-row gap (B59, B13, B51, B10) and in the diffuser passage (1 to 11). Actually they are distributed over the whole circumference of the machine but, for clarity of presentation, are brought together here as if they were located in a single diffuser passage. Figure 5 gives the location of the sensors in a meridional view of the compressor stage. Figure 6 shows a pressure sensor (sensor P4) mounted in the diffuser shroud.

Unsteady pressure measurements were collected at various stable operating points distributed along the  $\Omega_R$  iso-rotation speed curve (blue circles in Figure 7) and during slow throttle ramps into surge.

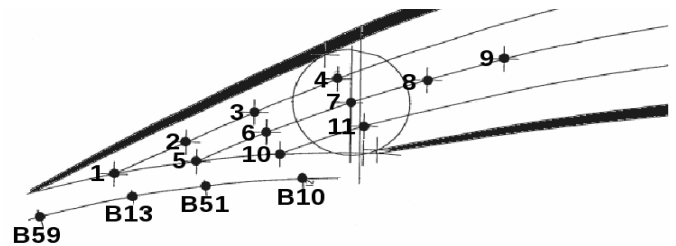


Figure 4. Location of the pressure sensors in the vaneless space (B59, B13, B51, B10) and in the diffuser passage (1 to 10).

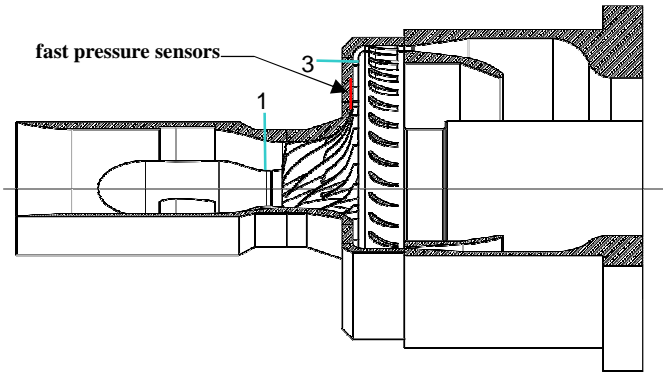


Figure 5. Location of the pressure sensors in a meridional view

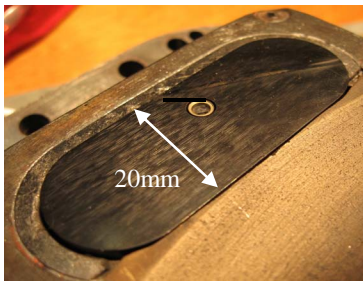


Figure 6. Pressure sensor P4

## NUMERICAL SIMULATION

The computations were performed with the elsA software developed at ONERA, which is more precisely described by Cambier and Gazaix [12]. The code solves the compressible RANS equations associated with the two equations ( $k-l$ ) turbulence model of Smith [13] on multi-block structured grids. The equations are discretized in the relative rotating frame using the Jameson's centered space scheme in a "cell-centered" approach. In order to stabilize the scheme, 2nd order and 4th order dissipative terms are added at the 4 steps of the Runge-Kutta time-integration scheme. An implicit residual smoothing technique is added to this explicit scheme.

For the impeller-diffuser interaction computation, the phase lagged approach is used. In this approach, the computation domain is limited to a single blade passage for each row. Assuming that there are no external unsteady causes, the unsteady effects are only due to the rotation. Then, the flow is time-periodic in the frame of reference of each row. As a consequence, a phase-lag exists between two adjacent blade passages. For each row, this phase-lag is the time taken by a blade of the next row to cover the pitch of the row. Basically, the phase-lagged technique consists in storing the flow values on the periodic boundaries and on the impeller-diffuser interface boundaries in order to deal with the phase-lag existing between adjacent blade passages.

The time needed to get an acceptable convergence varied from 100 hours CPU on NEC-SX8 for a peak efficiency

operating point up to 400 hours for an operating point near surge.

## Mesh

A multi-domain approach on structured meshes with H, C and O topologies is used. The near-wall region around the blades is described with  $y^+ < 3$ , to allow a precise description of the viscous effects and to capture the turbulent gradients. The tip clearance is meshed with an O-H topology to provide a good connection with blocks around the blades. To limit the memory requirement during computations the periodic interfaces are placed in the main blade and vane thickness.

The complete stage mesh used a multi-block strategy including 2,000,000 nodes in the impeller and 750,000 nodes in the diffuser.

## OVERALL PERFORMANCES

Figure 7 gives the pressure ratio curves coming from the unsteady calculations (marked with red squares) and the experiments as a function of the specific mass flow, at rotor speed  $\Omega_R = 0.927 \cdot \Omega_{nom}$ . The pressure ratio is defined as  $\pi = p_3/p_{t1}$ , and the reduced mass flow as:

$$\dot{m}_{red} = \frac{\dot{m} \sqrt{\gamma r T_{t1}}}{D_{IS}^2 p_{t1}} \quad (1)$$

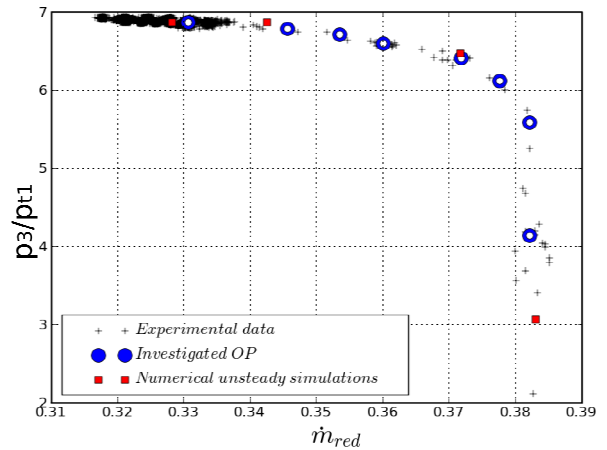


Figure 7. Pressure ratio of the compressor stage.

The experimental value of  $p_3$  is the mean value of the static pressures measured on the shroud and hub wall surfaces at the stage outlet (cf. Figure 5). The numerical values come from data extracted in the same sections. The mean numerical values come from time and area-averaged values.

The blue circles in Figure 7 show the operating points at which the unsteady pressure measurements were collected.

An excellent agreement between the unsteady numerical results and the experiments is found over the whole operating range. The last operating point which was converged is obtained at a mass flow slightly greater than the experimental surge limit. In order to reach a better agreement between the numerical surge limit and the experimental one, numerous and difficult calculations are necessary which would lead to drastically increase the numerical resources. That was not the purpose of the current study.

The good agreement between the numerical results and the experiments which is obtained for the overall performances is confirmed regarding the internal flow pattern which was also investigated by Laser Doppler Anemometry at peak efficiency [14] and near surge [15] (results not shown in this paper) and with the fast pressure sensors. For example, Figure 8 gives the ensemble-averaged pressure signals measured (red line) and extracted from the simulations (black line) near the vane suction side at the throat of the vaned diffuser (sensor P4, cf. Figure 4). Three sets of signals are given at three stable operating points: at choke ('C' at the top of Figure 8), at peak efficiency ('PE' in the middle) and near surge ('NS' at the bottom). The x-axis represents the time divided by the rotor main blade passing period

$$t^* = \frac{t}{T_R} = t \frac{\Omega_R N_R}{2\pi}$$

temporal fluctuations,  $p'$ , with the same scale for the three sets. The numerical extraction consists in inserting a virtual probe in the numerical field in order to take into account the spatial integration effect of the real probe. It is worth noticing that the numerical and experimental pressure signals are very similar whatever the operating point. In each signal, the four main fluctuations are generated by the pressure waves brought about by the interaction between the vane bow shock wave and the impeller main and splitter blades. These pressure waves, named  $\alpha^+$ , are particularly visible in Figure 9 which gives the pressure fluctuation  $p'$  (reduced by a reference value) in a time / space plot over two stator pitches (abscissa) and one and half rotor main blade passing period (ordinate), at mid inter row gap and 50% section height, at peak efficiency. The waves  $\alpha^+$  are generated in the vicinity of a metal coincidence (when a rotor blade and a diffuser vane are face-to-face) and move at a mean rotational speed of  $1.76 \Omega_R$ . During a main blade passing period four waves (marked with white circles in Figure 9) are registered at a given spatial position: two come from the reflection of the shock wave on the main blade and splitter blade pressure surfaces whereas the two others come from the reflection of the shock wave on the blades belonging to the adjacent former passage.

The numerical results being evaluated trustworthy, the flow pattern obtained at the last converged operating point (last stable point) is used in addition to the high frequency pressure signals in order to explain the scenario of the surge onset. But before that, the description of the evolution of the flow feature

from choke to surge is given in the diffuser which proved to be the component with the strongest pre-stall activity.

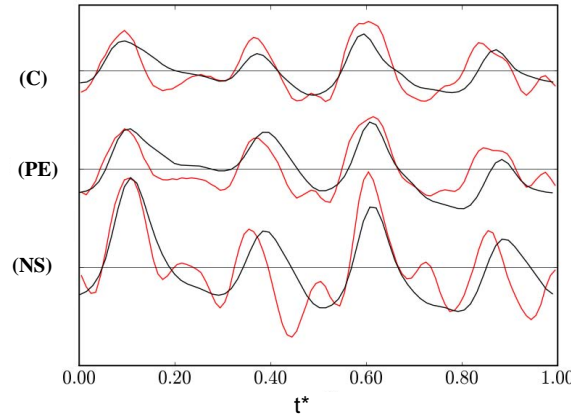


Figure 8. Numerical (black) and experimental (red) pressure signals near the vane suction side (sensor P4).

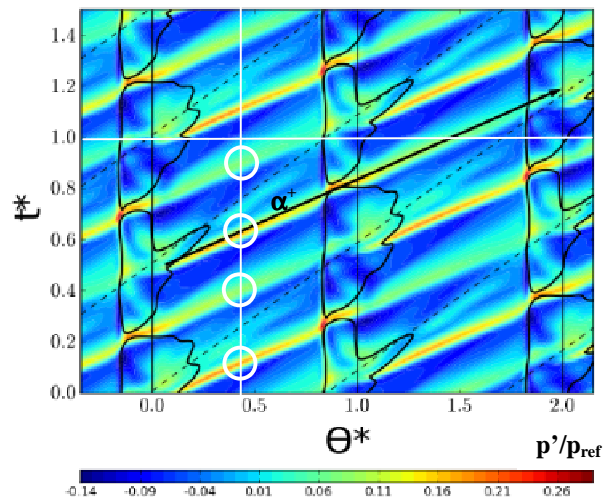
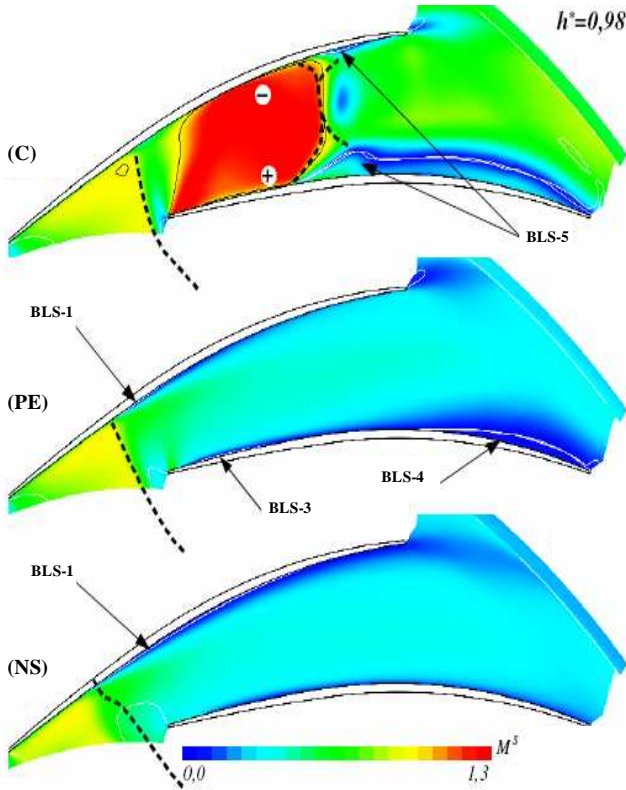


Figure 9. Time/space map of unsteady pressure contours at mid inter row gap and 50% section height, at peak efficiency.

## FLOW FEATURE IN THE DIFFUSER

Figure 10 depicts the evolution of the flow feature in the diffuser from choke to surge. The absolute Mach number time-averaged in the absolute frame of reference is drawn at 98% of section height. This section height is chosen because the results are further analyzed together with the pressure signals collected on the shroud. The dotted black curves mark the shock waves. The white lines give the zero-velocity contours.

At choke (top of Figure 10), the flow is supersonic at the diffuser throat. The supersonic area ends with a  $\lambda$ -shock which causes the boundary layer to separate on pressure and suction sides (BLS-5 in Figure 10), the separation being more pronounced on the pressure side.



**Figure 10.** Absolute Mach number in the diffuser at 98% section height for three operating points (top: choke ; middle : peak efficiency ; bottom: near surge).

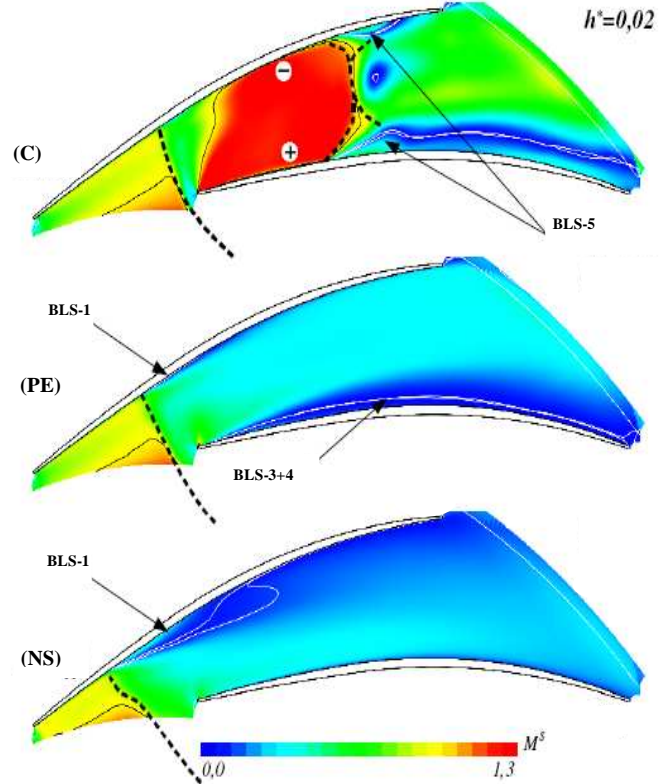
At peak efficiency (middle of Figure 10), the vane leading edge shock wave is strong leading to a subsonic flow downstream. The boundary layer separates on the vane pressure side. The boundary layer separation named BLS-3 results from the flow incidence whereas the boundary layer separation BLS-4 is due to the convex curvature of the vane pressure surface.

Near surge (bottom of Figure 10), the shock wave has moved upstream compared to the previous case. Due to the interaction between the shock wave and the suction side- shroud corner boundary layer, there is a separation (named BLS-1) on the vane suction side.

Therefore, from choke to surge, it may be concluded that:

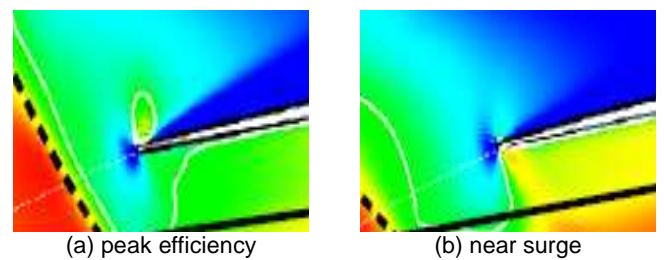
- the shock wave moves upstream,
- the throughflow trajectory moves from the vane suction side towards the vane pressure side,
- the boundary layer separation transfers from the pressure side to the suction side.

Figure 11 shows the flow pattern at 2% section height with the same scale as used in Figure 10. It is worth noticing that, near surge, the separation zone BLS-1 is larger near the hub because of the accumulation of low momentum fluid coming from the wake (of the jet-wake flow structure) which is transported towards the hub [16]. But whatever the section height, the conclusions written above are confirmed.



**Figure 11.** Absolute Mach number in the diffuser at 2% section height for three operating points (top: choke ; middle : peak efficiency ; bottom: near surge).

Let us now zoom in on the flow at the vane leading edge. Figure 12 gives the absolute Mach number very close to the vane leading edge, at peak efficiency and near surge. The dotted black lines and the white curves mark the detached bow shock wave and the sonic contours respectively.



**Figure 12.** Absolute Mach number at the diffuser leading edge, at 50% section height.

At peak efficiency (Figure 12-a), the flow around the leading edge is fully subsonic. Near surge, the incoming flow is more tangential than the vane at the leading edge. The flow deflection imposed by the vane leading edge leads to an increase in Mach number on the vane suction side, very close to the leading edge. One may thus notice a little expansion zone followed by a weak oblique shock (Figure 12-b). The

contribution of this weak oblique shock enhances as the compression system moves to surge. For clarity, this weak oblique shock is further named secondary shock whereas the detached bow shock is named primary shock.

**PRESSURE SIGNALS IN THE VANELESS SPACE**

Figure 13 shows four pressure signals measured by the sensors B-59, B-13, B-51 and B10 located at mid-vaneless space during a surge cycle. The abscissa is the time reduced by the rotor main blade passing period. The white curves give the pressure values which result from a time-average over a rotor revolution and afterwards written as  $\tilde{p}^{RR}$ .

The surge cycle period is governed by the air circuit. In the present case, the surge cycle period is equal to around 10000 blade passing period. Any given surge cycle may be decomposed into two stages. In a first stage, the compression system breaks: the instantaneous pressure value may reach four times the reference value which is almost the mean pressure within the vaneless diffuser before surge. The  $\tilde{p}^{RR}$  value increases rapidly at the beginning of this stage, and then decreases to the same value whatever the considered sensor. At the same time, the pressure fluctuations are considerably attenuated. The low level of the pressure (instantaneous values

and  $\tilde{p}^{RR}$  values) allows the compression system to restore to normal working: that is the second stage of the surge cycle.

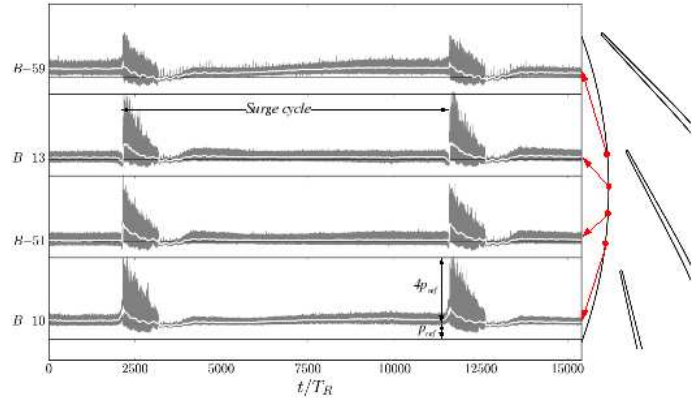


**Figure 13.** Pressure signals during a surge cycle obtained by sensors B-59, B-13, B-51 and B10 located at mid-vaneless space.

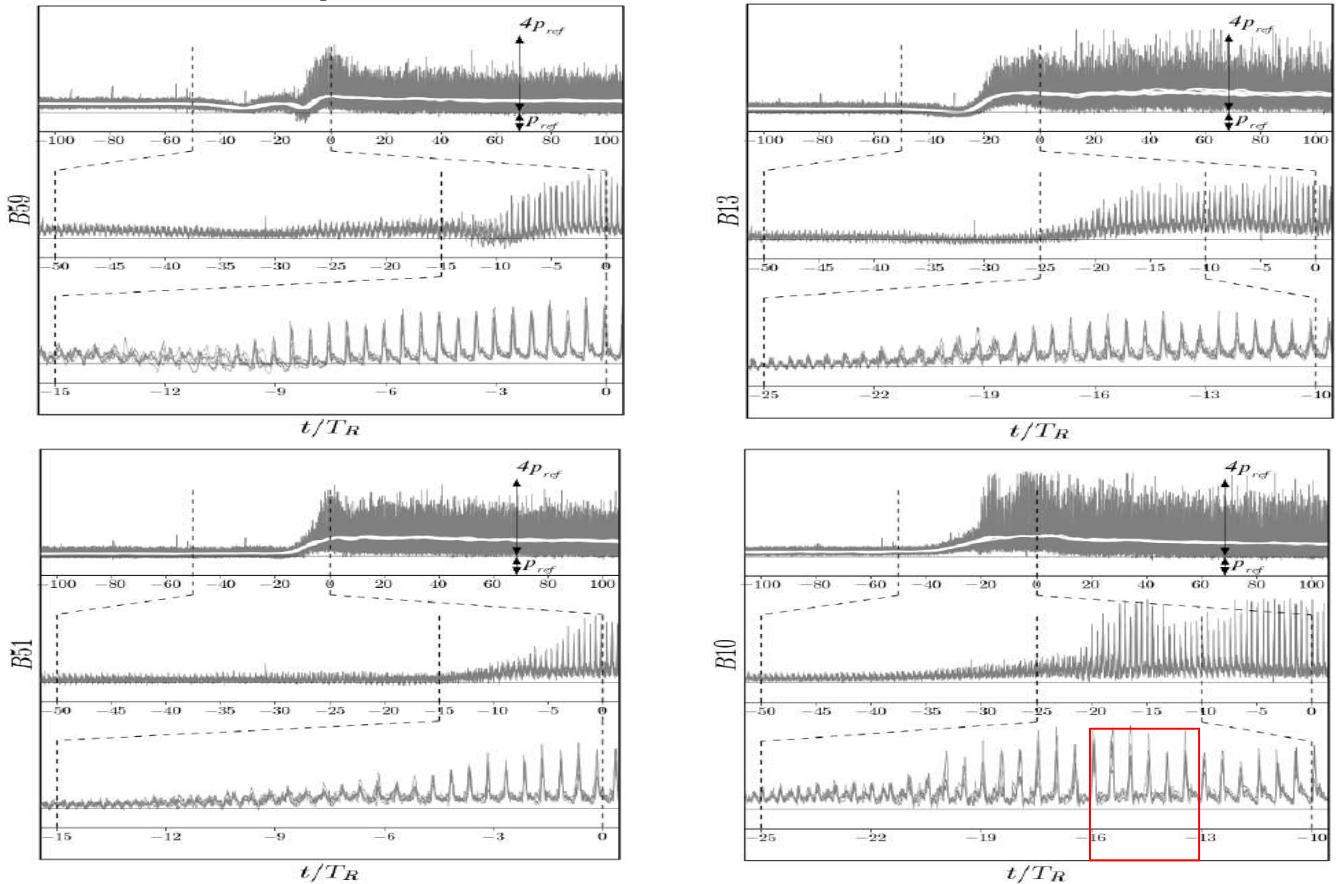


**Figure 14.** Pressure signals from the sensors B-59, B-13, B-51 and B10 during surge onsets

Figure 14 focuses on the surge onset (beginning of the first stage). It gives the signals acquired by the sensors B-59, B-13, B-51 and B10 during six different surge onsets. The six signals which are superimposed were shifted in time in order to fix the surge onset modulo a blade passing period. The signals are then twice zoomed in on the surge onsets.

No pre-surge activity is noticed before around fifty times the blade passing period, it means before  $5 \cdot 10^{-3}$  second.

The  $\tilde{p}^{RR}$  values obtained for the six rough signals (white curves) are very well superimposed. An impressive superimposition is also achieved for the instantaneous signals whatever the considered sensor (that is all the more noticeable in the zooms). It may therefore be concluded that:

- the surge inception is a repeatable process (i.e. not governed by random flow structures),
- the temporal fluctuations are synchronized with the blade passing. For example, six peaks occur over three main blade periods (marked with a red square in Figure 14), which leads to a period of the signal equals to  $T_R/2$ . It is interesting to remember that before surge the pressure signals were characterised by a period of  $T_R/4$  resulting from the pressure waves  $\alpha^+$  (cf. Figure 8).

### PRESSURE SIGNALS IN THE DIFFUSER PASSAGE

Figure 15 gives the pressure signals coming from the sensors B51 and P7 during the surge onset. These sensors are selected because B-51 is the less sensitive to the diffuser (due to its location) whereas P7 is located at mid-throat of the diffuser.

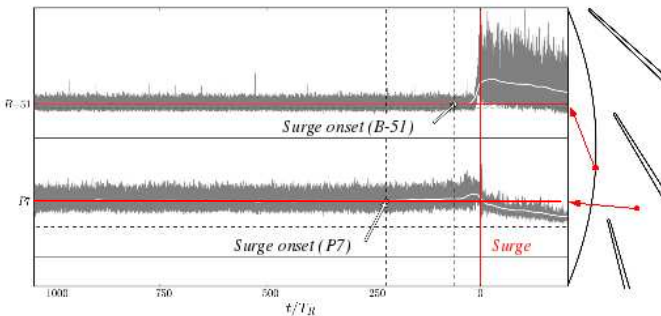


Figure 15. Pressure signals during a surge onset obtained by the sensors B-51 and P7.

The  $\tilde{p}^{RR}$  value (white line) obtained at the location P7 reveals a slight shift compared with the mean value before surge (red line) 150 times the main blade passing period before the sensor B-51. That excludes the rotor to be the source of the compression system break because the first pre-surge activity is detected at the diffuser throat. That is also confirmed by the signals acquired by sensors located at the rotor leading edge on the shroud endwall which never show any pre-surge activity before the downstream sensors.

In the diffuser, the weakest flow zone near surge is located in the vicinity of the vane suction side, where the boundary layer separation named BLS-1 was detected (cf. Figures 10 and 11). In order to investigate this zone, the signals coming from the sensors B-59, P1, P2, P3 and P4 are analysed in Figure 16.

The surge onset is decomposed into three steps.

- The first step corresponds to a slight increase in the  $\tilde{p}^{RR}$  value at the location P4, and then moving upstream from the locations P4 to B-59.
- The second step lasts a very short time. It is characterized by a rapid increase in the  $\tilde{p}^{RR}$  value at the sensors P1, P2, P3 and P4, whereas the pressure decreases at the location B-59.
- The third step begins when the  $\tilde{p}^{RR}$  values at the sensors P1, P2, P3 and P4 reach their highest levels. Afterwards, a decrease in the temporal fluctuations is clearly visible at the locations P2, P3 and P4. Finally, a sudden and strong increase in the instantaneous pressure at the location B-59 is recorded which triggers the surge properly speaking.

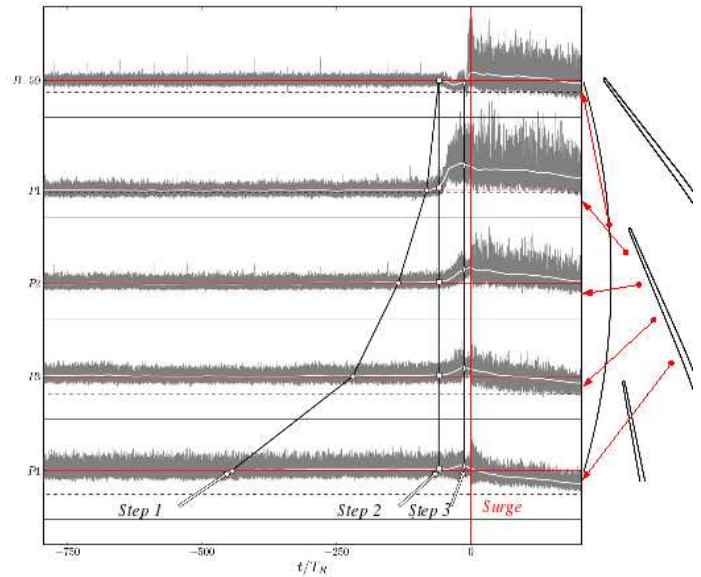


Figure 16. Pressure signals during a surge onset obtained by the sensors B-59, P1, P2, P3 and P4.

### THE SURGE ONSET SCENARIO

The slight increase in the  $\tilde{p}^{RR}$  value at the sensor P4 (cf. Figure 16) is the first pre-surge sign that can be noticed. It appears around 500 times the blade passing period before the compression system breaks, it means around  $5 \cdot 10^{-2}$  second before surge. This pressure increase results from the vane suction side boundary layer separation due to the shock wave / boundary layer interaction (named BLS-1 in Figures 10 and 11).

This separation may be considered as the start of a series which lead to surge, as described below.

The separation bubble leads to an increase in the flow incidence at the diffuser inlet (the flow is more tangential). The increase in incidence causes an increase in Mach number by the expansion wave due the change in flow direction. The increase in Mach number causes the enlargement of the separation bubble (because the shock wave / boundary layer interaction becomes stronger) which leads the primary shock to move upstream. The increase in Mach number also causes the oblique shock (secondary shock in Figure 12) to strengthen. Little by little, the secondary shock and the primary shock merge together. A new supersonic pattern is therefore obtained in the diffuser entry zone. It is very unstable because the compression system breaks less than 25 times the blade passing period later.

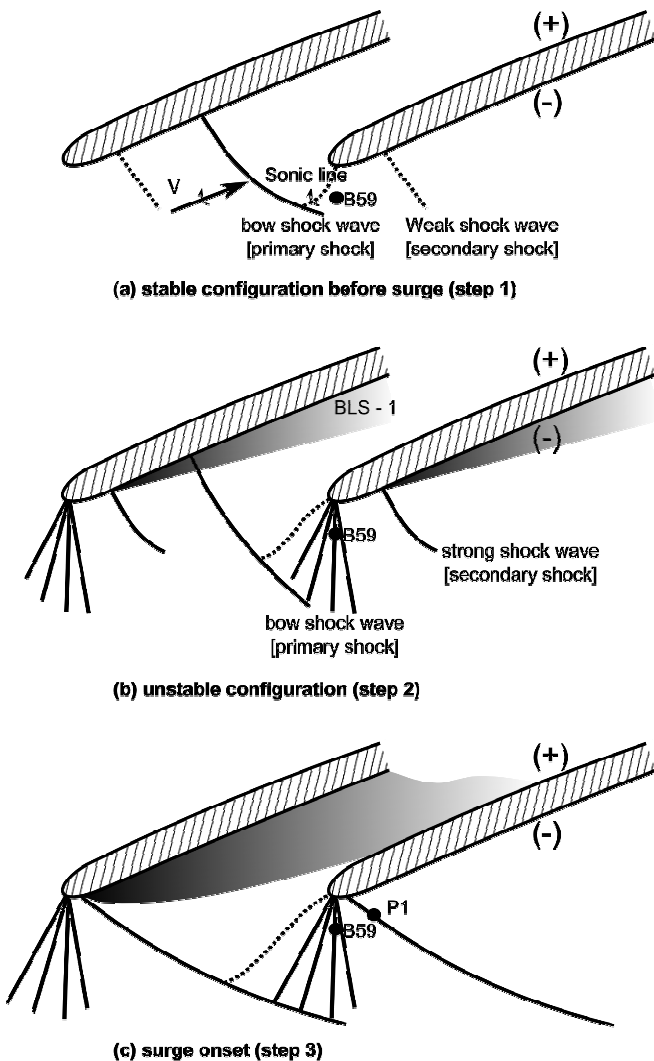


**Figure 17.** Sketch of the flow pattern close to the vane leading edge from stable configuration to surge.

Figure 17 gives a sketch of the flow pattern in the vicinity of the vane leading edge during this process.

Figure 17-a shows the flow pattern at a stable operating point before surge. It is characterized by a strong detached bow shock (primary shock) and a weak oblique shock (secondary shock), as seen in Figure 12.

In figure 17-b, the incoming flow has rotated towards positive incidence, leading to an expansion wave at the suction side. The oblique shock (secondary shock) has thus been strengthening. That explains why the  $\tilde{p}^{RR}$  value at the sensor B-59 decreases whereas the  $\tilde{p}^{RR}$  values at the sensors P1, P2, P3 and P4 increase during the step 2 (cf. Figure 17). Indeed, the sensor B-59 is located in the expansion wave whereas the sensors P1, P2, P3 and P4 are located behind the secondary shock.

As the separation zone BLS-1 enlarges, the primary shock moves upstream then merges with the secondary shock (Figure 17-c). The resulting configuration is very unstable (step 3 lasts less than 25 times the blade passing period) and represents the ultimate flow pattern before surge. Therefore the surge properly speaking could be the result of the massive blockage in the diffuser entry (Figure 17-c) or a break of the ultimate shock system which would enable the reverse flow originally located in the vane suction side – endwall corners to move upstream. Until now no available data can discriminate one or the other situation. Actually, the description of the path to surge was the objective of the present work and not the surge itself.

#### ADDITIONAL COMMENTS

The pressure signals are characterised by the traces of the waves  $\alpha^+$  which are the most important structures involved in the impeller-diffuser interaction [17]. These waves result from the reflection of the vane leading edge shock wave on the rotor blade pressure surface. At a stable operating point, the waves strengthen near the vane suction side when moving in the vane passage due to the concave shape of the suction surface. That explains the increase in intensity of the pressure signal from the sensor P1 to the sensor P4 (cf. Figure 16). When moving towards surge, the vane shock wave moves upstream and the shock pattern changes from the configuration (a) to the configuration (c), (Figure 17). Due to the strengthening of the shock, the intensity of the waves  $\alpha^+$  increases. A major change in the signals concerns the frequency which is divided by two from a stable operating point to surge (cf. Figures 8 and 14): it is thought that the waves coming from the interaction of the shock with the blades of the adjacent passage are weakened by the expansion wave. The frequency of the signal during surge is thus the frequency of the blade passing ( $2/T_R$ ).

The flow emerging from the impeller is distorted because of combined effects of curvatures, rotation and tip leakage flow. This distortion leads to the classical 'jet and wake' structure which, as it moves, is responsible of a periodic increase in

Mach number ahead of the bow shock wave. Therefore the shock wave periodically fluctuates upstream of the vane channels. This is thought to be the reason of the high level of fluctuations registered at surge at the sensor P1 which is thus located in the shock (Figures 16 and 17-c).

## CONCLUSION

A combined analysis of numerical and experimental results led to achieve a comprehensive description of the flow in a high-pressure centrifugal compressor stage used in a helicopter engine from choke to surge. The main change in the flow pattern is in the diffuser: the boundary layer separates on the vane pressure side at choke and at peak efficiency operating point whereas it separates on the vane suction side near surge. The vane suction side thus reveals to be the weakest zone in term of flow stability. A detailed examination of the time-dependent pressure signals then led to propose the path to surge. First, it is interesting to note that the surge inception revealed to be a perfectly repeatable process, synchronized with the blade passing period. When moving towards surge, the increase in flow incidence generates a new pattern of shock and expansion waves together with an enlargement of the separated zone within the diffuser. This resulting configuration is very unstable (it lasts less than 25 times the blade passing period) and represents the ultimate flow pattern before surge.

The pre-surge behaviour is thus characterised by short-wavelength perturbations which are inherent to the supersonic flow conditions. The further step of this work is to investigate the surge onset at lower rotation speeds with subsonic flow conditions.

## ACKNOWLEDGMENTS

We would like to thank TURBOMECA which supported this research.

G. Halter, B. Paoletti, P. Laucher and S. Goguey are acknowledged for experimental support.

This work was performed using HPC resources from GENCI [CCRT/CINES/IDRIS] (Grant2009- [i2010026356]).

## REFERENCES

- [1] **Z. S. Spakovszky**, 2000, "Applications of Axial and Radial Compressor Dynamic System Modeling", Thesis, Massachusetts Institute of Technology, Department of Aeronautics and Astronautics.
- [2] **Z. S. Spakovszky**, 2004, "Backward Traveling Rotating Stall Waves in Centrifugal Compressors", *Journal of Turbomachinery*, vol. 126, pp. 1-12.
- [3] **M. P. Wernet, M. M. Bright et G. J. Skoch**, 2001, "An Investigation of Surge in a High-Speed Centrifugal Compressor Using Digital PIV", *Journal of Turbomachinery*, vol. 123, pp. 418-428.
- [4] **G. J. Skoch, G. P. Herrick, M. D. Hathaway, J. Chen et R. S. Webster**, 2005 "Technology for Stabilizing the Compression System of a US Army Helicopter Gas Turbine Engine: Validation of Unsteady Simulations", *Proceedings of the American Helicopter Society 61st Annual Forum*, Grapevine, USA.
- [5] **F. Justen, K. U. Ziegler et H. E. Gallus**, 1999, "Experimental Investigation of Unsteady Flow Phenomena in a Centrifugal Compressor Vaned Diffuser of Variable Geometry", *Journal of Turbomachinery* vol.121, pp. 763-771.
- [6] **Z. S. Spakovszky et C. H. Roduner**, "Spike and Modal Stall Inception in an Advanced Turbocharger Centrifugal Compressor", *Journal of Turbomachinery*, 2009, vol. 131, pp.1-9.
- [7] **H. Hayami, Y. Senoo et K. Utsunomiya**, 1990, "Application of a Low-Solidity Cascade Diffuser to Transonic Centrifugal Compressor", *Journal of Turbomachinery*, vol.112, pp. 25-29.
- [8] **H. Hayami, M. Sawae, T. Nakamura et N. Kawaguchi**, 1993, "Blade Loading and Shock Wave in a Transonic Circular Cascade Diffuser", *Journal of Turbomachinery*, vol. 115, pp. 560-564.
- [9] **D. Bonaiuti, A. Arnone, C. Hah et H. Hayami**, 2002, "Development of Secondary Flow Field in a Low Solidity Diffuser in a Transonic Centrifugal Compressor Stage", *Proceedings of the International Gas Turbine Institute*, Amsterdam, Netherlands.
- [10] **I. Trébinjac, P. Kulisa, N. Bulot, N. Rochuon**, 2009, "Effect of the Unsteadiness on the Performance of a Transonic Centrifugal Compressor Stage" *J. Turbomach.* -- October 2009 -- Volume 131, Issue 4, 041011 (9 pages).
- [11] **N. Bulot, X. Ottavy, I. Trébinjac**, 2010, "Unsteady Pressure Measurements in a High-Speed Centrifugal Compressor " *Journal of Thermal Science*, Science Press, Vol.19, N°1, pp.1-8.
- [12] **L. Cambier et M. Gazaix**, 2002, "elsA: an Efficient Object-Oriented Solution to CFD Complexity", *Proceedings of the 40th Aerospace Science Meeting and Exhibit*, Reno, USA.
- [13] **B.R. Smith**, 1994, "Prediction of Hypersonic Shock Wave Turbulent Boundary Layer Interactions with the k-l Two-Equation Turbulence model". *AIAA Paper 95-02232*, 33rd ASME, Reno, NV
- [14] **N. Rochuon**, 2007, "Analyse de l'écoulement tridimensionnel instationnaire dans un compresseur centrifuge à fort taux de pression". Ph.D. thesis, Ecole Centrale de Lyon, n°2007-05
- [15] **N. Bulot, I. Trébinjac, X. Ottavy, P. Kulisa, G.Halter, B.Paoletti, P.Krikorian**, 2009, "Experimental and Numerical Investigation of the Flow Field in a High-

Pressure Centrifugal Compressor Impeller near Surge", IMechE Journal of Power and Energy, Volume 223, Number 6, pp.657-666.

- [16] **N. Bulot et I.Trébinjac**, 2009, "Effect of the Unsteadiness on the Diffuser Flow in a Transonic Centrifugal Compressor Stage," International Journal of Rotating Machinery, vol. 2009, Article ID 932593, 11 pages.
- [17] **N. Bulot et I.Trébinjac**, 2007, "Impeller-diffuser interaction: analysis of the unsteady flow structures based on their direction of propagation", Journal of Thermal Science, Science Press, Vol.16, N°3, pp.193-202.